



Chen, G., Tang, L. and Yu, Z. (2020) Underlying mechanisms of limit-cycle, beating and quasi-periodic oscillations in thermoacoustic devices. *Journal of Physics D: Applied Physics*, 53(21), 215502. (doi: [10.1088/1361-6463/ab7a57](https://doi.org/10.1088/1361-6463/ab7a57)).

This is the author's final accepted version.

There may be differences between this version and the published version. You are advised to consult the publisher's version if you wish to cite from it.

<http://eprints.gla.ac.uk/209802/>

Deposited on: 10 February 2020

Enlighten – Research publications by members of the University of Glasgow
<http://eprints.gla.ac.uk>

Underlying mechanisms of limit-cycle, beating and quasi-periodic oscillations in thermoacoustic devices

Geng Chen^{1, 2}, Lihua Tang^{1,*}, Zhibin Yu^{2,*}

1. Department of Mechanical Engineering, University of Auckland, 20 Symonds Street, Auckland 1010, New Zealand

2. James Watt School of Engineering, University of Glasgow, Glasgow G12 8QQ, UK

Correspondence: l.tang@auckland.ac.nz and Zhibin.Yu@glasgow.ac.uk

ABSTRACT

Under certain circumstances, spontaneous acoustic oscillations inside thermoacoustic systems exhibit beating and quasi-periodic patterns, in contrast to constant-amplitude limit-cycle oscillations regularly studied in the literature. This paper explores the underlying mechanisms of limit cycles, beating and quasi-periodicity in thermoacoustic devices from acoustic/vibrational and thermodynamic/hydrodynamic perspectives. Firstly, the acousto-mechanical coupling between the thermoacoustic engine (TAE) and external load is investigated using a lumped element model (LEM), which is verified against a distributed parameter model (DPM). The effect of external load on the natural frequencies and mode shapes of intrinsic oscillation modes is investigated. Secondly, the thermoacoustic coupling between the temperature and acoustic fields is analysed using a reduced-order network model based on the linear thermoacoustic theory. The effect of thermoacoustic core on stability of oscillation modes is studied. Finally, the steady-state behaviour of the device is examined by considering the unsteady linear decay/growth and nonlinear saturation processes. This study demonstrates that the linear mode selection decides whether the steady state is static (quiescent) or dynamic. Apart from linear mode selection, the dynamic steady-state responses are also affected by nonlinear mode competition during the saturation process. Simultaneous excitement of oscillation modes at different external loads may lead to distinctively different steady-state waveforms including beating and quasi-periodicity. Discussions on the steady-state energy transition/conversion indicate that, to improve the performance of the thermoacoustic device, excitation of the oscillation mode whose frequency is close to that of the external load is encouraged. It is suggested that ultra-compliant transducers be employed for better acoustic power extraction.

Keywords: Thermoacoustic engine; Beating; Quasi-periodicity; Lumped element model; Network model;

1. Introduction

Thermoacoustic engines (TAEs) or prime movers are natural heat engines capable of converting external heat, such as industrial waste heat, solar energy, excess heat from microelectronic devices, etc.,

into acoustic oscillations through the thermoacoustic effect [1-6]. The thermoacoustics is a multidisciplinary research topic that blends the knowledge of thermodynamics, heat transfer, fluid mechanics, vibration, acoustics, dynamics, to name a few. It was first qualitatively explained by Lord Rayleigh (so-called Rayleigh's stability criterion [7]), then theoretically (linear theory) investigated by Rott [8] through perturbation of Navier-Stokes equations, and later advanced by Swift and his colleagues [9-11] by incorporating one more total energy equation. Targeting at industrial design and practical application of thermoacoustic apparatuses, Swift et al. [12] further developed a computer programme called DeltaEC (Design Environment for Low-amplitude ThermoAcoustic Energy Conversion), which has gained popularity in the thermoacoustic research community.

Despite the existence of a linear theory, complex phenomena in thermoacoustic devices are frequently encountered and not fully understood. These phenomena in the literature can be classified into four main categories based on the existing research fields. First introduced are the nonlinear effects in fluidic field, which normally include multi-dimensional flow effects [13], minor losses caused by vortex shedding [14], mass streaming [15], onset of turbulence [16], and so on. Second, at large-amplitude thermoacoustic oscillations, complex acoustic phenomena such as harmonic distortions [17] and shock waves [18] may appear. Another group of complex behaviour is related to nonlinear dynamics. Examples of such phenomena include hysteresis [19-21], chaotic oscillations [22], mode transition [23], phase-locking and amplitude death (or quenching) due to synchronization [24-26], etc. The last type of complex observations in thermoacoustic engines is called periodic switching/surging [27-29], a phenomenon that involves the energy transition between the heat storage in the stack/regenerator and acoustic energy of the oscillating fluid. The “double-threshold effect [30]” and “fishbone-like instability [31]” are also believed to share the same underlying energy conversion mechanism.

Another two interesting complex phenomena observed in thermoacoustic devices are beating and quasi-periodicity, which are rarely reported and thus less familiar to researchers. In regular operational conditions, the steady-state pressure waveforms are limit cycles with a stabilized invariant pressure amplitude. However, it was reported by Yazaki [32-34], Atchley [35] and Sujith [36] that the limit-cycle acoustic oscillations inside the thermoacoustic systems became quasi-periodic as the temperature gradient imposed on the stack increased. Similar quasi-periodic patterns were also observed in a recent study by Chen [3] where a piezoelectric membrane was used to harvest energy from the thermoacoustic engine. What's more, Wang [37] noticed that the beating oscillations occurred if the natural frequency of the mechanical subsystem (i.e., linear alternator) was tuned to be the same as the resonance frequency of the thermoacoustic oscillator. Up till now, although experimentally investigated, the beating and quasi-periodicity phenomena inside thermoacoustic systems have not been theoretically addressed, and the basic principles governing these effects still remains unclear.

Thermoacoustic engines are essentially the acoustic equivalents of conventional gas-cycle engines. They rely on the complex interactions between the gas parcels and the solid boundaries (at microscopic level) in the thermoacoustic core (i.e., a piece of porous material with a steep axial temperature gradient) to facilitate the thermodynamic/hydrodynamic processes and induce spontaneous acoustic oscillations. The design and control of geometrical/thermophysical parameters and boundary conditions have great influence on the dynamic behaviour of spontaneous acoustic oscillations, and therefore are pivotal for the operation and optimization of thermoacoustic systems. As reviewed above, different dynamic waveforms such as limit cycles, beating and quasi-periodicity have been observed in the past decades, but no generic theory has been developed to explain the differences. Therefore, this study aims at developing an analytical approach to comprehend the underlying mechanisms of various dynamic waveforms in thermoacoustic devices. Efforts are made towards the modelling and analysis of the acousto-mechanical and thermo-acoustic coupling effects which play an important role on the dynamic characteristics of thermoacoustic oscillations.

The rest of the paper is organized as follows. [Section 2](#) introduces the thermoacoustic device investigated in this study. Background information of coupling types and dynamic responses of the device below and above onset is provided. [Section 3](#) describes the lumped element model for studying the intrinsic acoustic oscillation modes inside the thermoacoustic device. [Section 4](#) presents the network model that selects the unstable oscillation modes in the linear regime. Following the linear mode selection, the unsteady transition to steady-state oscillations is analysed in [Section 5](#). [Section 6](#) discusses the steady-state energy transition and conversion. Finally, concluding remarks are drawn in [Section 7](#).

2. Problem formation

2.1 Model description

[Figure 1](#) shows a representative thermoacoustic device where a standing-wave thermoacoustic engine (TAE) is integrated with an external load [\[38\]](#). The TAE is composed of a hot buffer, a stack and an acoustic resonator. The external load, simplified as a single mechanical oscillator in the figure, could be in the form of a piston [\[39\]](#), a mechanical-to-electric transducer [\[40\]](#), acoustic radiation [\[41\]](#), or even a thermoacoustic refrigerator [\[42\]](#). The key geometrical parameters of the TAE in this study are listed in [Table 1](#). The working fluid inside the engine is air (ideal gas) at atmospheric pressure ($p_m = 101,325$ Pa). High-amplitude standing waves are first initiated and sustained inside the air-filled TAE in the presence of a large temperature gradient across the parallel-plate thermoacoustic stack that is sandwiched between a pair of hot and cold heat exchangers. Subsequently, the acoustic oscillations inside the acoustic resonator are absorbed by the external load, producing useful mechanical work, electricity, or refrigeration (cold energy), etc. Thereby, energy conversion from heat to other forms of energy is realized by the thermoacoustic device.

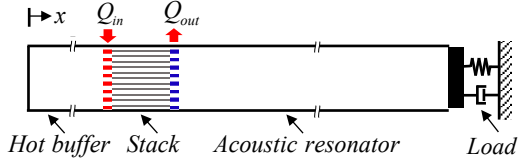


Figure 1. Schematic of a thermoacoustic device which comprises a standing-wave thermoacoustic engine and an external load.

Table 1. Key geometrical parameters for the standing-wave thermoacoustic engine.

Parameters	Values
Diameter D	0.05 m
Hot buffer length L_H	0.1 m
Stack length L_S	0.04 m
Resonator length L_R	0.36 m
Stack plate thickness t_s	8×10^{-4} m

2.2 Coupling types

In general, there are two distinctively different types of coupling effects inside a thermoacoustic device. One is the acousto-mechanical coupling between the acoustic waveguide (e.g. feedback loop, acoustic resonator, etc.) and external load. This process concerns the sound propagation and reflection, and therefore determines the intrinsic acoustic oscillation modes as will be discussed in [Section 3](#). The other coupling type is the thermo-acoustic coupling between acoustic and temperature fields at the fluid/solid interfaces where non-zero time-averaged hydrodynamic entropy and work flows arise because of the thermoacoustic effect. Sound generation or absorption is involved in this process. It will be found in [Section 4](#) that this process is also responsible for deciding the most unstable oscillation modes (linear mode selection).

In this paper, for simplicity, a linear-type standing-wave TAE employing a parallel-plate stack ([Figure 1](#)) is chosen to study the above two coupling effects. The more complicated looped-type TAE using a thermoacoustic regenerator (e.g., Stirling-type TAE) will be investigated in the future.

2.3 Evolution of pressure disturbances

In thermoacoustic systems, “positive feedback” inside the inhomogeneous thermoacoustic core (i.e., stack or regenerator) relies on the phase shifts within the penetration depths, leading to non-isentropic oscillations. The difference between resultant time-averaged entropy flows entering and leaving the working fluid contributes to a net time-averaged work flow (acoustic power) that combats the viscous and thermal losses in the rest of the whole device. The temperature gradient across the thermoacoustic core plays an important role in the acoustic power generation and thereby the dynamic responses of initial pressure disturbances.

At small temperature gradients, acoustic power generation is smaller than dissipation: pressure disturbances attenuate, as shown in Figures 2(a) and 2(b). Quantitative values of pressure amplitude P_A and acoustic power are not of interest and therefore not given. As time goes by, the evolution of pressure disturbances below onset experiences two consecutive processes: (i) initial decay where the system is unsteady and P_A decreases exponentially with time at a constant decay rate. Both acoustic power generation and dissipation are proportional to P_A^2 (initial value $P_{A,ini}^2$) in this linear regime [1]; (ii) static steady state (from $t = t_S$) where P_A decreases to zero and the system is quiescent. At large temperature gradients, acoustic power generation exceeds dissipation: onset of instability takes place, as shown in Figures 2(c) and 2(d). The evolution of pressure disturbances above onset normally contains three consecutive processes: (i) initial growth where the system is linearly unstable/unsteady. P_A increases exponentially with time at a constant growth rate; (ii) saturation where the system is still unsteady. However, the growth rate decreases due to nonlinear viscous/thermal losses; (iii) dynamic steady state (from $t = t_S$) where the growth rate is zero and dynamic energy balance is achieved between acoustic power generation and dissipation.

It should be noted that the waveforms exemplified in Figures 2(a) and 2(c) are sinusoidal oscillations at a single frequency. Here come three questions. Is it possible that beating or quasi-periodic patterns occur? How will the two coupling categories mentioned above affect the dynamic responses? Does the saturation process affect the steady-state waveforms? These questions will be addressed in next sections.

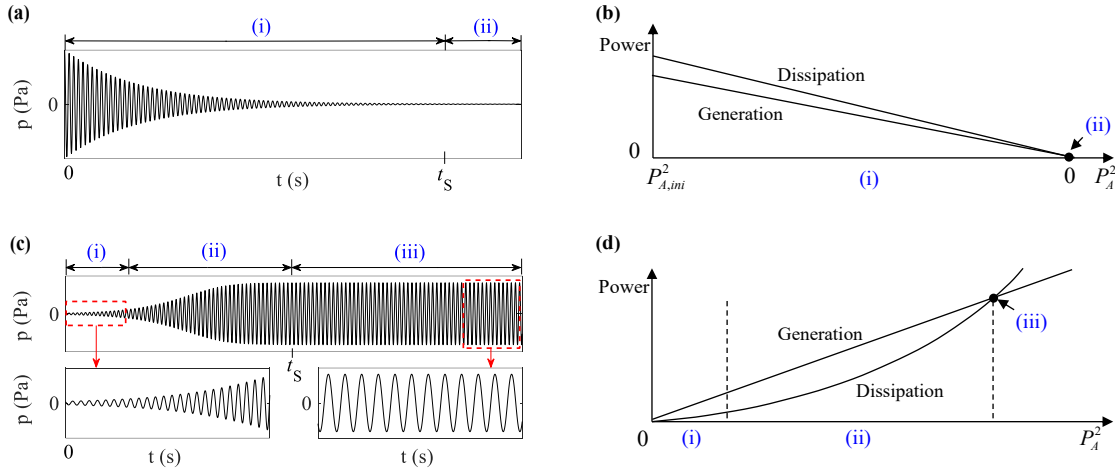


Figure 2. Evolution of pressure disturbances. (a) Pressure oscillations decaying with time below onset. (b) Hypothesised relationship between the acoustic power generation and dissipation below onset. (c) Self-excited pressure oscillations evolving into limit cycles above onset. (d) Hypothesised relationship between the acoustic power generation and dissipation above onset.

3. Intrinsic oscillation modes

In the first place, thermoacoustic systems are acoustic systems. The oscillation nature of a thermoacoustic system offers the feasibility of studying the sound propagation or reflection from a pure acoustic/vibrational perspective. This section investigates the effect of acousto-mechanical coupling on the intrinsic (acoustic) oscillation modes inside the thermoacoustic device displayed in [Figure 1](#).

3.1 Lumped element model

By using the perturbation techniques, Swift derived the linearized quasi-one-dimensional continuity and momentum equations in thermoacoustics [\[1\]](#). For the working fluid inside the TAE with length Δx , the volume velocity and acoustic pressure differences at the ends can be expressed by

$$\Delta U_1 = - \left(j\omega c_{omp} \Delta x + \frac{1}{r_k} \Delta x \right) p_1 + g \Delta x U_1 \quad (1)$$

$$\Delta p_1 = -(j\omega l \Delta x + r_v \Delta x) U_1 \quad (2)$$

where $j = \sqrt{-1}$ is the imaginary unit and ω is the angular frequency. p_1 and U_1 denote the first-order expansion values of acoustic pressure and volume velocity.

$$c_{omp} = \frac{S}{\gamma p_m} (1 + (\gamma - 1) \Re[f_k]), \quad l = \frac{\rho_m}{S} \frac{1 - \Re[f_v]}{|1 - f_v|^2} \quad (3)$$

represent the acoustic compliance and inertance per unit length, respectively.

$$\frac{1}{r_k} = \frac{\gamma - 1}{\gamma} \frac{\omega S \Im[-f_k]}{p_m}, \quad g = \frac{f_k - f_v}{(1 - f_v)(1 - \sigma)} \frac{1}{T_m} \frac{dT_m}{dx}, \quad r_v = \frac{\omega \rho_m}{S} \frac{\Im[-f_v]}{|1 - f_v|^2} \quad (4)$$

represent the thermal-relaxation resistance per unit length, complex gain/attenuation constant due to a non-zero temperature gradient and viscous resistance per unit length, respectively. p_m , ρ_m and T_m are the mean pressure, density and temperature of the working fluid. S is the cross-sectional area of the flow channel ($S_1 = S/2$ in the stack region), σ is the Prandtl number and γ is the ratio of isobaric to isochoric specific heats. $f_{v,k}$ are thermo-viscous functions accounting for the thermo-acoustic coupling at the fluid/solid interfaces [\[43\]](#). $\Re[\]$ and $\Im[\]$ denote the real and imaginary parts of a complex quantity.

Motivated by Swift's work, we establish a multi-degree-of-freedom (MDOF) model of the thermoacoustic device by evenly dividing the TAE into sub-segments with length Δx : the number of sub-segments of the hot buffer, stack and resonator are n_1 , $n_2 - n_1$ and $n_3 - n_2$, respectively. Tests show that $\Delta x = 5$ mm is small enough for the results to converge. As illustrated in [Figure 3](#), the working fluid inside the TAE is represented by a number of mechanical oscillators in series, and the external load is simplified as a single mechanical oscillator. The equivalent stiffness, mass, damping coefficient,

displacement around equilibrium positions of each degree of freedom (DOF) are denoted by K , M , c and w , respectively. Note that $K = S^2 \Delta x / c_{omp}$ and $M = S^2 \Delta x l$. Different from the thermoacoustic refrigerator (TAR) where the working fluid is forced by an external actuator (e.g., loudspeaker) with designated amplitude and frequency, the thermoacoustic engine, in contrast, is self-excited where the damping coefficient c of each DOF is determined by the joint influence of $1/r_k$, g and r_v . Analogous to negative damping at large wind speeds leading to galloping [44], large temperature gradients will induce negative damping in the stack region ($c_{n1+1}, \dots, c_{n2} < 0$) that counteracts the positive damping within the hot buffer ($c_1, \dots, c_{n1} > 0$), resonator ($c_{n2+1}, \dots, c_{n3+1} > 0$) and external load ($c_M > 0$).

From the above analysis, we can see that K , M and c of the working fluid are all affected by $f_{v,k}$ if the thermo-acoustic coupling is considered. However, since this section primarily focuses on the derivation of intrinsic oscillation modes, we assume negligible thermo-acoustic coupling ($f_{v,k} = 0$) and only consider the effect of acousto-mechanical coupling. This assumption is valid because the near-wall penetration depths are very small compared to the hydraulic radius of hot buffer and resonator. Moreover, the length of the stack is small compared to that of the whole device or acoustic wavelength, although the penetration depths are relatively large in the stack region. Therefore, the equivalent stiffness, mass and damping coefficient of the each DOF are simplified and expressed as

$$M \approx \rho_m S \Delta x; \quad K \approx \gamma p_m S / \Delta x; \quad c = 0 \quad (5)$$

As to the external load, the equivalent mechanical impedance can be written as

$$Z_L = j\omega M_M + K_M / (j\omega) + c_M \quad (6)$$

Our previous study [41] shows that c_M has negligible impact on the oscillation modes and thereby neglected ($c_M = 0$). Under these assumptions, the MDOF model in Figure 3 is simplified to an “undamped free vibration” model, which is also referred to as the lumped element model (LEM) in this study.

To summarize, the key features of the lumped element model are as follows. (i) $f_{v,k}$ and c_M are omitted. (ii) T_m is constant at 300 K along the TAE. (iii) ω is real since there is no resistance considered. (iv) Both frequency-domain and time-domain analyses (shown later) are available.

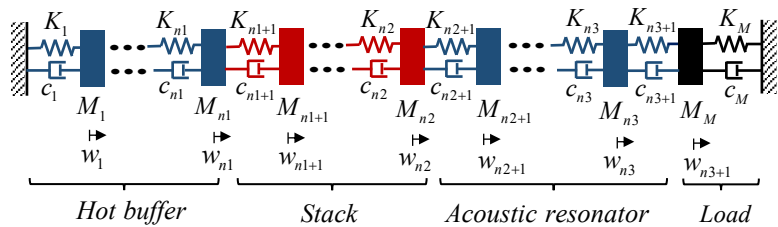


Figure 3. Generic MDOF representation of the TAE integrated with an external load.

3.2 Eigenvalue problem

The governing equations for the lumped element model can be written as

$$\mathbf{M}\ddot{\mathbf{w}} = \mathbf{0} \quad (7)$$

where

$$\mathbf{M} = \text{diag}(M_1 \ M_2 \ \cdots \ M_{n_3+1} \ M_M); \mathbf{K} = \begin{bmatrix} K_1 + K_2 & -K_2 & \cdots & \cdots & 0 \\ -K_2 & K_2 + K_3 & & \ddots & \vdots \\ \vdots & & \ddots & & \vdots \\ \vdots & & \ddots & K_{n_3} + K_{n_3+1} & -K_{n_3+1} \\ 0 & \cdots & \cdots & -K_{n_3+1} & K_{n_3+1} + K_M \end{bmatrix} \quad (8)$$

are the mass and stiffness matrices. And

$$\ddot{\mathbf{w}} = \begin{bmatrix} \ddot{w}_1 & \ddot{w}_2 & \cdots & \ddot{w}_{n_3} & \ddot{w}_{n_3+1} \end{bmatrix}^T \quad \mathbf{w} = [w_1 \ w_2 \ \cdots \ w_{n_3} \ w_{n_3+1}]^T \quad (9)$$

are the acceleration and displacement vectors. Assuming harmonic time dependence, Equation (7) can be rewritten as

$$[-\mathbf{M}\omega^2 + \mathbf{K}]\mathbf{w} = \mathbf{0} \quad (10)$$

which has nontrivial solutions if

$$|-\mathbf{M}\omega^2 + \mathbf{K}| = 0 \quad (11)$$

Solving the above characteristic equation yields the eigenvalues ω_i^2 and natural frequencies ω_i ($i = 1, \dots, n_3+1$) of each longitudinal oscillation mode. The eigenvector ϕ_i (or mode shape) for each longitudinal oscillation mode can then be obtained by solving the following equation

$$(\mathbf{K} - \omega_i^2 \mathbf{M})\phi_i = \mathbf{0}; \quad i = 1, 2, \dots \quad (12)$$

Note that the natural frequencies can be also derived using a distributed parameter model (DPM) in [Appendix A](#). The natural frequencies obtained from the two methods agree with each other very well, which validates the lumped element method applied in this study.

3.3 Natural frequencies and mode shapes

[Figure 4](#) shows the effect of external load stiffness K_M on the natural frequencies of the first three oscillation modes while keeping M_M constant at M_b using the lumped element model. The baseline values of mass and stiffness of the external load are set at $M_b = 0.01$ kg and $K_b = 1 \times 10^4$ kg/s², respectively. Similar patterns can be found on the effect of external load mass M_M when K_M is kept constant at K_b , and therefore not displayed herein.

In Figure 4, the natural frequency $f_M = (K_M/M_b)^{0.5}$ of the external load alone increases with the increase of K_M . When K_M/K_b is small (e.g., around 1), the first (fundamental) natural frequency f_1 of the coupled system (i.e., the TAE with external load) is close to that of the external load, whereas the second and third mode frequencies f_2 and f_3 of the coupled system approximate the natural frequencies $f_{\text{TAE}1}$ and $f_{\text{TAE}2}$ of the TAE alone corresponding to a wavelength λ of $2L$ and L , respectively. When K_M/K_b reaches around 4.5, f_1 and f_2 become close but f_3 barely changes. As K_M/K_b increases to around 12, f_1 and f_3 approximate $f_{\text{TAE}1}$ and $f_{\text{TAE}2}$, while f_2 approximates f_M . When K_M/K_b reaches 20, f_1 barely changes, but f_2 is close to f_3 . Finally, when K_M/K_b increases to 30, f_1 and f_2 approximate $f_{\text{TAE}1}$ and $f_{\text{TAE}2}$, whereas f_3 approximates f_M .

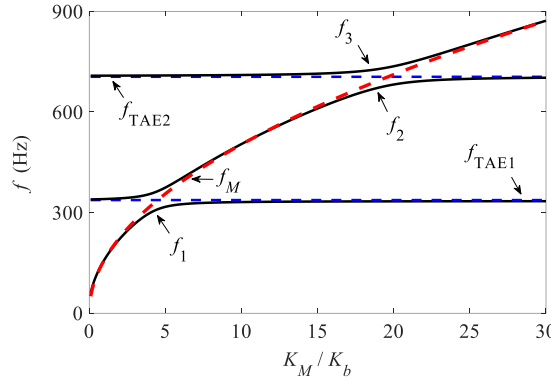


Figure 4. Effect of external load stiffness K_M on the first, second and third mode frequencies (solid lines) of the thermoacoustic device. f_M (dashed red line) is the natural frequency of the external load. $f_{\text{TAE}1}$ and $f_{\text{TAE}2}$ (dashed blue lines) are natural frequencies of the TAE.

Figure 5 presents the longitudinal mode shapes ϕ_1 , ϕ_2 and ϕ_3 at a few selected values of K_M/K_b using the lumped element model. The shaded areas indicate the location of the stack where cross-sectional area suddenly decreases ($S_1 = S/2$). w_i is normalized (divided by maxima) at each oscillation mode. In the figure, the right-end displacement is almost zero at oscillation modes whose frequencies approximate $f_{\text{TAE}1}$ and $f_{\text{TAE}2}$. However, large non-zero displacements at the right end are observed at the fundamental mode in Figure 5(a), the second mode in Figure 5(c) and the third mode in Figure 5(e). These oscillation modes (highlighted) have frequencies close to f_M . It is also observed in Figures 5(b) and 5(d) that, oscillation modes with close frequencies share similar mode shapes (highlighted) and have small non-zero right-end displacements.

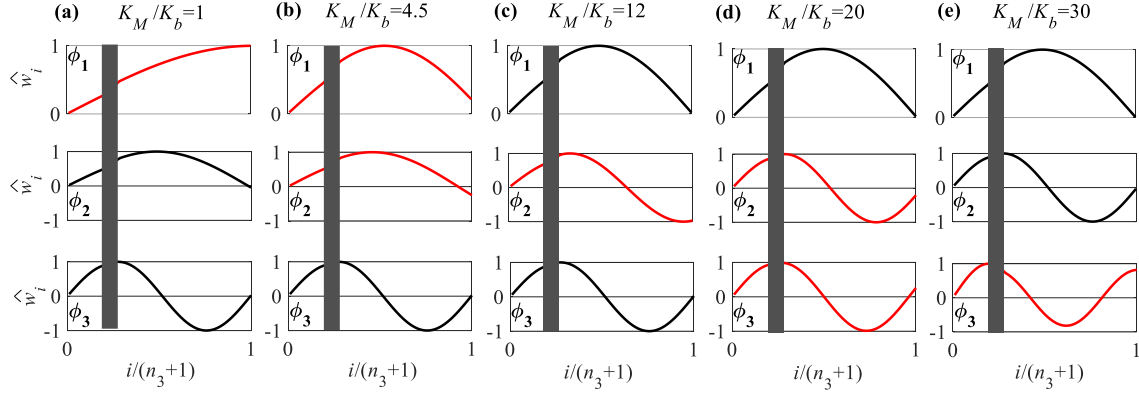


Figure 5. Longitudinal mode shapes at (a) $K_M/K_b = 1$; (b) $K_M/K_b = 4.5$; (c) $K_M/K_b = 12$; (d) $K_M/K_b = 20$; (e) $K_M/K_b = 30$. Highlighted oscillation modes have obvious non-zero right-end displacements.

4. Linear mode selection

Thermoacoustic systems are also thermodynamic systems where non-zero time-averaged acoustic power is generated or dissipated in each thermodynamic cycle due to the thermoacoustic effect. Following the pure acoustic/vibrational analysis of intrinsic oscillation modes, this section proceeds to investigate the stability of oscillation modes from a thermodynamic/hydrodynamic viewpoint by considering the thermo-acoustic coupling effect.

4.1 Network model

In this work, a system-level reduced-order network model based on the linear thermoacoustic theory [1] is utilized to conduct the stability analysis. Detailed descriptions of this method could be found in our previous study [3]. Note that, different from LEM, non-zero thermo-viscous functions $f_{v,k}$ associated with thermo-acoustic coupling and mechanical resistance of the external load are included in the network model: c_{omp} and l in Equation (3) and $1/r_k$, g and r_v in Equation (4) are used; c_M is described by $2\xi(K_M M_M)^{0.5}$, where ξ is the damping ratio, chosen to be 0.001.

Figure 6 illustrates the detailed configuration of a parallel-plate thermoacoustic stack. The key parameters are hydraulic radius r_h which is half of the gap between the stack plates, and the thermal penetration depth $\delta_k = (2\kappa/\rho_m c_p \omega)^{0.5}$ where κ and c_p are thermal diffusivity and isobaric specific heat of the fluid. A linear temperature distribution (from T_h to T_c) is imposed on the solid surfaces and the cold-end temperature T_c of the stack is maintained at 300 K. The temperatures of the hot buffer and acoustic resonator are assumed constant at T_h and T_c , respectively. The temperature dependences of dynamic viscosity μ and thermal conductivity κ follow Sutherland's laws [45]. As to the boundary conditions of the TAE, a solid wall is imposed at the left end ($x = 0$) whereas at the right end ($x = L$), impedance matching applies between the equivalent acoustic impedance $Z_A = Z_L/S^2$ of the external load and that of the working fluid. Hence, the characteristic equation from the network model becomes [3]

$$M_{T21}Z_A - M_{T11} = 0 \quad (13)$$

where M_{T11} and M_{T21} are first-column elements of the total transfer matrix \mathbf{M}_T . Solving the characteristic equation yields the complex frequency $\omega = \omega_R + j\omega_I$ as a function of hot-end temperature T_h for each oscillation mode. The onset temperature $T_{h,\text{onset}}$ and onset frequency $\omega_{\text{onset}}/2\pi$ are determined when ω_I is zero.

To summarize, the key features of the network model are as follows. (i) $f_{v,k}$ and c_M are non-zero. (ii) T_m is not constant along the TAE. (iii) ω is complex and dependent on T_h . (iv) Only frequency-domain analysis is available.

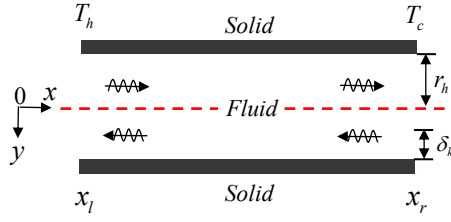


Figure 6. Diagram of two adjacent plates in a parallel-plate thermoacoustic stack.

4.2 Stability curves

Figures 7(a) to 7(e) display the stability curves of oscillation modes calculated from the network model at $K_M/K_b = 1, 4.5, 12, 20$ and 30 , respectively. r_h varies from 0.18 mm to 0.8 mm. Geometrical dimensions of the TAE in Table 1 are adopted. In each figure, stability curves of oscillation mode(s) whose right-end displacement is no-zero are highlighted. It is found that, at each oscillation mode, the onset temperature $T_{h,\text{onset}}$ is minimum when r_h is neither too small nor too large. Appendix B shows that minimum $T_{h,\text{onset}}$ is obtained when the non-dimensional parameter r_h/δ_k lies around 1.6 , where the longitudinal time-averaged enthalpy flux h_x peaks. This proves the fact that the thermoacoustic stack relies on irreversible heat conduction to produce acoustic power whereas at two reversible processes (isothermal or adiabatic) when r_h is extremely small or large, acoustic power generation disappears.

Generally, oscillation modes with higher frequencies possess higher $T_{h,\text{onset}}$. However, this does not apply to oscillation modes highlighted due to high mechanical resistance from the external load. As seen in Figure 7(a) where $K_M/K_b = 1$, the stability curves of the first and second oscillation modes intersect. In region (I), no oscillation modes are excited. Any initial pressure disturbances will be damped. In region (II), only the fundamental oscillation mode is unstable while in region (III), only the second oscillation mode is prone to becoming unstable. In regions (IV) and (V), the first two and all first three oscillation modes can be initiated. In Figure 7(b) where $K_M/K_b = 4.5$, since f_1 and f_2 are close, the corresponding stability curves are close: the area of region (II) shrinks significantly. In Figure 7(c) where $K_M/K_b = 12$, $T_{h,\text{onset}}$ at the second oscillation mode increases remarkably due to large non-zero displacement of the external load. In Figure 7(d) where $K_M/K_b = 20$, the second and third oscillation

modes have close stability curves because f_2 and f_3 are close. In Figure 7(e) where $K_M/K_b = 30$, the stability curve of the third oscillation mode is above 2000 K (not practical) and not displayed.

To conclude, from the stability analysis, one can find that multiple oscillation modes can be excited/damped simultaneously if both parameters T_h and r_h lie within certain regions. In other words, the thermoacoustic stack selects the linearly unstable oscillation modes according to T_h and r_h .

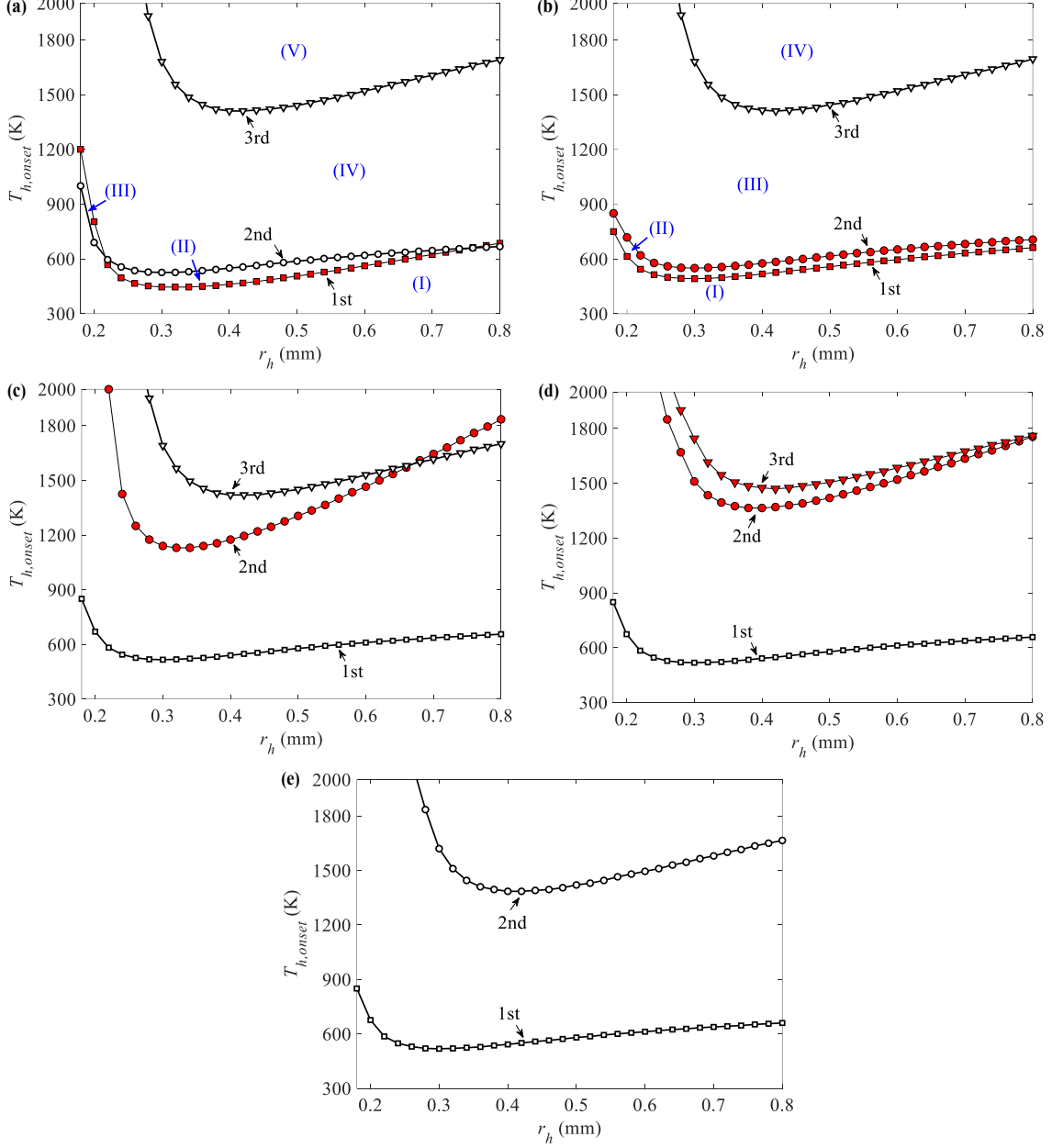


Figure 7. Stability curves of oscillation modes at (a) $K_M/K_b = 1$; (b) $K_M/K_b = 4.5$; (c) $K_M/K_b = 12$; (d) $K_M/K_b = 20$; (e) $K_M/K_b = 30$. Highlighted stability curves correspond to oscillation modes with obvious non-zero right-end displacements.

5. Unsteady transition to steady state

The linear mode selection determines the excitation/suppression of oscillation modes at instant $t = 0$. This section discusses the unsteady transition from $t = 0$ to $t = t_s$ (see Figure 2). In addition, approximate time-domain solutions to the steady-state dynamics are presented. Finally, experimental evidences reported in the literature are provided to support theoretical predictions.

5.1 Unsteady transition

5.1.1 Linear decay below onset

As discussed in Section 2.3, one possible steady state is quiescence after the linear decay process below onset. From Figure 7, we realize that if T_h and r_h fall within region (I), any oscillation mode(s) excited initially, for example, by an external disturbance, will be damped afterwards. The waveform in Figure 2(a) illustrates the case in which one single oscillation mode is damped. However, it will be shown in Section 5.4 that the waveform changes when multiple oscillation modes are damped simultaneously.

5.1.2 Linear growth and nonlinear saturation above onset

Another possible steady state is dynamic energy balance after the linear growth and nonlinear saturation processes above onset. If T_h and r_h fall within region (IV) or (V) in Figure 7(a), multiple oscillation modes will be triggered simultaneously. The waveform in Figure 2(c) only corresponds to the case where one single oscillation mode is initiated.

In the linear growth process, the oscillation modes do not interfere with each other at small amplitudes. However, in the unsteady, large-amplitude saturation process, the nonlinear nature of oscillations encourages mode competition and energy cascade from one mode to another. Such complex behaviour has been observed in previous experimental work [32-35]. A recent study also shows that when the TAE is operating in the large-amplitude regime, nonlinear excitation of higher harmonics could even induce shock waves [46]. So far, the principle of nonlinear mode competition in thermoacoustic devices is still unclear. In order to investigate the complex nonlinear interaction between oscillation modes, one may resort to nonlinear acoustics/thermoacoustics, which is out of scope for this study that is primarily interested in trends rather than precise agreement. Quantitative analysis on the growth rates of oscillation modes during the nonlinear saturation process will be conducted in future studies.

5.2 Approximate steady-state solutions

5.2.1 Static steady state

If the static steady state (quiescence) is achieved after the linear decay process below onset, the approximate solution of the steady-state displacement vector will be $\mathbf{w} = \mathbf{0}$.

5.2.2 Dynamic steady state

Following the lumped element model in [Section 3](#), the MDOF system first is decoupled and the governing equations are rewritten as

$$[-\mathbf{M}_p \omega^2 + \mathbf{K}_p] \mathbf{w}_p = \mathbf{0} \quad (14)$$

where

$$\begin{cases} \mathbf{M}_p = \boldsymbol{\phi}^T \mathbf{M} \boldsymbol{\phi} = \text{diag}(M_{p1} \ M_{p2} \ \dots \ M_{pn_3} \ M_{pM}) \\ \mathbf{K}_p = \boldsymbol{\phi}^T \mathbf{K} \boldsymbol{\phi} = \text{diag}(K_{p1} \ K_{p2} \ \dots \ K_{pn_3} \ K_{pM}) \\ \mathbf{w}_p = [w_{p1} \ w_{p2} \ \dots \ w_{pn_3} \ w_{p(n_3+1)}]^T \end{cases} \quad (15)$$

are the principal mass matrix, stiffness matrix and displacement vector at the principal coordinate.

$$\boldsymbol{\phi} = [\boldsymbol{\phi}_1 \ \dots \ \boldsymbol{\phi}_{n_3+1}] \quad (16)$$

is the modal matrix of the coupled system. The time-domain solution of [Equation \(14\)](#) is

$$w_{pi} = w_{pi}(0) \cos(\omega_i t^*) + i \dot{w}_{pi}(0) \sin(\omega_i t^*) / \omega_i; \quad i = 1, 2, \dots \quad (17)$$

where $t^* = 0$ starts from $t = t_s$. $w_{pi}(0)$ and $\dot{w}_{pi}(0)$ are initial conditions ($t^* = 0$) at the principal coordinate that are determined by the initial displacement vector $\mathbf{w}(0)$ and velocity vector $\dot{\mathbf{w}}(0)$, i.e.,

$$\mathbf{w}_p(0) = \boldsymbol{\phi}^{-1} \mathbf{w}(0); \quad \dot{\mathbf{w}}_p(0) = \boldsymbol{\phi}^{-1} \dot{\mathbf{w}}(0) \quad (18)$$

Then, by considering the joint influence of linear mode selection and nonlinear mode competition, $\mathbf{w}(0)$ and $\dot{\mathbf{w}}(0)$ can be described by superposition of unstable oscillation modes, i.e.,

$$\mathbf{w}(0) = \sum_{i=1}^{n_3+1} \beta_i \boldsymbol{\phi}_i; \quad \dot{\mathbf{w}}(0) = \sum_{i=1}^{n_3+1} \beta_i \dot{\boldsymbol{\phi}}_i \quad (19)$$

where β_i are the steady-state mode coefficients that reflect the extent to which an oscillation mode is excited. Since only first three oscillation modes could possibly be excited in the steady state, $\beta_4, \dots, \beta_{n_3+1}$ are set at zero in the following calculations. The values of β_1, β_2 and β_3 vary case by case, as will be discussed in the next section. Finally, the approximate time-domain solution to the steady-state displacement vector \mathbf{w} is derived and expressed by

$$\mathbf{w} = \boldsymbol{\phi} \mathbf{w}_p \quad (20)$$

5.3 Experimental evidences

This section presents four examples showing distinctively different waveforms as a result of simultaneous excitement of oscillation modes at different K_M/K_b using the lumped element model.

5.3.1 Limit cycles

The first example is limit-cycle oscillations that exhibit sinusoidal waveforms at a single frequency. When T_h and r_h lie within region (II) at $K_M/K_b = 1$ in Figure 7(a), only the fundamental oscillation mode is excited. If we assume that the second and third oscillation modes have negligible contributions after the nonlinear saturation process, β_1 , β_2 and β_3 can be prescribed as 1, 0 and 0, respectively and the corresponding steady-state waveforms are displayed in Figure 8. The solid dots in the figure denote the positions where the waveforms are monitored. Limit-cycle oscillations at f_1 show up at all positions.

Steady-state limit-cycle oscillations are frequently encountered and investigated extensively in the literature. For example, Figure 9 displays one such pattern observed in our recent experimental study [4].

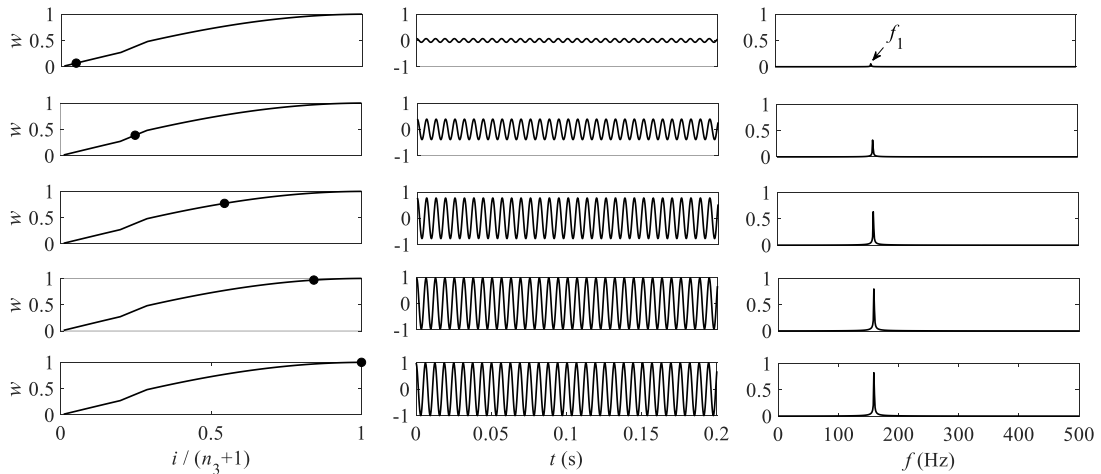


Figure 8. Steady-state limit-cycle oscillations at $K_M/K_b = 1$. $\beta_1 = 1$; $\beta_2 = 0$; $\beta_3 = 0$.

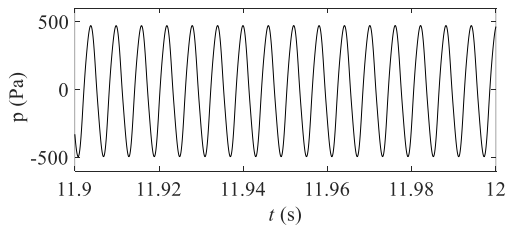


Figure 9. Experimental evidence of steady-state limit-cycle oscillations, from Chen et al. [4], reproduced with the permission of the John Wiley and Sons Ltd.

5.3.2 Quasi-periodicity

The second example discusses the overlapping of two unstable oscillation modes in region (IV) at $K_M/K_b = 1$ in Figure 7(a). In this case, the first and second oscillation modes have comparable dominance

and energy levels at the position of thermoacoustic stack. Without probing into the complex mode competition during saturation, we assume β_1 , β_2 and β_3 to be 1, 0.5 and 0, respectively. It is interesting to find that, the mode superposition at $K_M/ K_b = 1$ induces quasi-periodic oscillations as shown in Figure 10. It is interesting to find that, the influence of second oscillation mode diminishes as the monitored position moves towards the external load, as seen from the spectrum analyses. In particular, at the external load, the contribution of second oscillation mode is so small that the steady-state waveforms reduce to quasi-sinusoidal oscillations.

Simultaneous excitement of the first two oscillation modes in experiments was reported by Yazaki [32], Biwa [34], Atchley [35] and Sujith [36] etc. The steady-state, quasi-periodic waveforms are rare in experiments since high temperature gradients are required. Fortunately, we are able to find a similar pattern from Atchley et al. [35] as seen in Figure 11. The close match between the waveforms verifies the feasibility of the analytical method in this study.

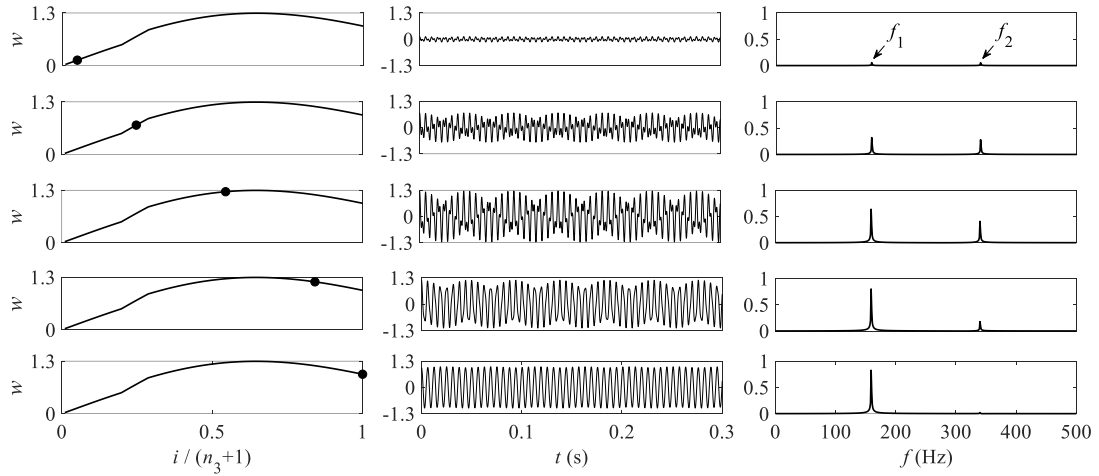


Figure 10. Quasi-periodic oscillations at $K_M/ K_b = 1$. $\beta_1 = 1$; $\beta_2 = 0.5$; $\beta_3 = 0$.

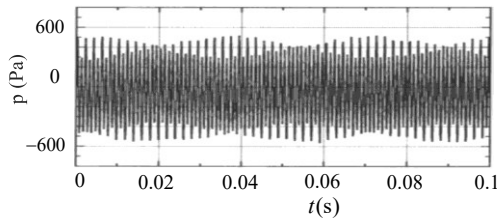


Figure 11. Experimental evidence of steady-state quasi-periodic oscillations, from Atchley et al. [35], reproduced with the permission of the Acoustical Society of America.

5.3.3 Beating

The third example concerns the occurrence of beating phenomenon in region (III) at $K_M/ K_b = 4.5$ in Figure 7(b). Since the first and second oscillation modes have close $T_{h,\text{onset}}$, they are almost equally excited in region (III) where the effect of third oscillation mode is assumed to be negligible. Thus, β_1 , β_2 and β_3 are set at 1, 1 and 0, respectively. Figure 12 depicts the predicted steady-state waveforms at

the positions of thermoacoustic stack and the external load. Beating effect occurs simultaneously at both positions: the displacement amplitude has a pulsing pattern (also termed “beats”) with the time difference between two adjacent peaks/troughs equal to $1/(f_2 - f_1)$. It is interesting to note that an increase of displacement amplitude at the stack position leads to a decrease of displacement amplitude at the external load.

Unfortunately, so far, we have not found any experimental proof of steady-state beating phenomenon in the literature. Nevertheless, as shown in [Figure 13\(a\)](#), the decaying beating effect was observed by Wang et al. [37] in a Stirling-type thermoacoustic system where the acoustic resonator and linear alternator have similar natural frequencies. We then realize that the case in Wang’s study falls within region (I) in [Figure 7\(b\)](#) where the first two oscillation modes are damped together. Multiplying [Equation \(17\)](#) with $e^{j\omega_l t}$ where ω_l is the decay rate (assumed as -25 rad/s herein), and following the same calculation steps, we are able to produce the decaying beating effect at the stack position, as shown in [Figure 13\(b\)](#), using our current theoretical model. Although the quantitative values differ due to different geometrical parameters, the beating pattern and decaying trend between the theoretical prediction and experimental data are qualitatively consistent with each other.

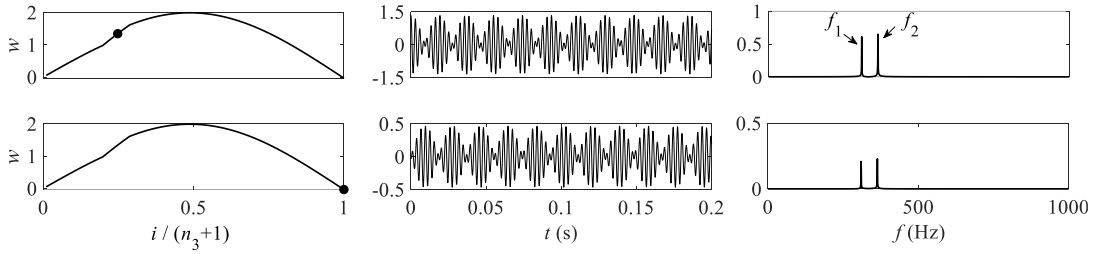


Figure 12. Steady-state beating oscillations at $K_M/ K_b = 4.5$. $\beta_1 = 1$; $\beta_2 = 1$; $\beta_3 = 0$.

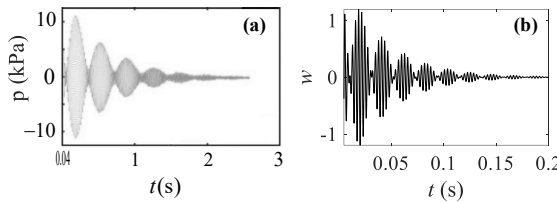


Figure 13. Experimental evidence of beating oscillations. (a) Experimental data from Wang et al. [37], reproduced with the permission of the American Institute of Physics. (b) Theoretical prediction.

5.3.4 Blend of beating and quasi-periodicity

The fourth example describes another possible scenario when the third oscillation mode is excited together with the first and second oscillation modes. Such scenario exists when T_h and r_h lie within region (IV) at $K_M/ K_b = 4.5$ in [Figure 7\(b\)](#). [Figure 14](#) illustrates the steady-state waveforms at the positions of thermoacoustic stack and the external load when β_1 , β_2 and β_3 are assumed as 1, 1 and 0.8, respectively. A mixture of three oscillation modes makes the waveforms at the stack position

complicated: quasi-periodic and beating oscillations co-exist. It can be inferred from Figures 10 and 12 that the quasi-periodic oscillations only dominates in the stack region while the beating phenomenon can exist at all positions. Thus, at the external load, the influence of the third oscillation mode diminishes and only beating effect remains. At present, there is no report of such patterns in previous experiments due to the need of extremely large temperature gradients that is hard to realize in practical implementations.

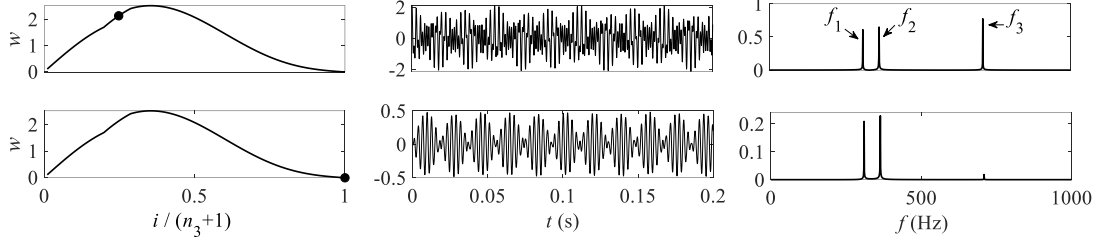


Figure 14. Blend of beating and quasi-periodic oscillations at $K_M/K_b = 4.5$. $\beta_1 = 1$; $\beta_2 = 1$; $\beta_3 = 0.8$.

6. Energy transition and conversion

6.1 Acousto-mechanical energy transition

To better understand the steady-state waveforms discussed above, the acousto-mechanical energy transition between the acoustic energy of the TAE and the mechanical energy of the external load is first studied. The term “energy transition” is adopted since the acoustic energy can be regarded as the mechanical energy of the working fluid.

By using the lumped element model, the instantaneous acoustic energy E_{TAE} stored in the TAE is expressed as a sum of kinetic energy (due to inertance) and potential energy (due to compressibility) of each lumped element, i.e.,

$$E_{TAE} = \underbrace{\frac{1}{2} \sum_{i=1}^{n_3} M_i \dot{w}_i^2}_{E_{k,TAE}} + \underbrace{\frac{1}{2} \sum_{i=1}^{n_3} K_{i+1} (w_{i+1} - w_i)^2}_{E_{p,TAE}} \quad (21)$$

where $E_{k,TAE}$ and $E_{p,TAE}$ denote total kinetic energy and potential energy of the TAE, respectively. Likewise, the instantaneous energy E_L stored in the external load is expressed by

$$E_L = \underbrace{\frac{1}{2} M_M \dot{w}_{n_3+1}^2}_{E_{k,L}} + \underbrace{\frac{1}{2} M w_{n_3+1}^2}_{E_{p,L}} \quad (22)$$

where $E_{k,L}$ and $E_{p,L}$ are the kinetic energy and potential energy of the external load. Then, the instantaneous total energy E_T of the entire thermoacoustic device is

$$E_T = E_{TAE} + E_L \quad (23)$$

Figure 15 displays the time histories of $\hat{E}_{k,TAE}$, $\hat{E}_{p,TAE}$ and \hat{E}_{TAE} (normalized by $E_{TAE,\max}$ where subscript “max” denotes the maximum value), $\hat{E}_{k,L}$, $\hat{E}_{p,L}$ and \hat{E}_L (normalized by $E_{L,\max}$), and \hat{E}_{TAE} , \hat{E}_L and \hat{E}_T (normalized by $E_{T,\max}$) in four representative conditions. In Figure 15(a), at $K_M/K_b = 1$, only the first oscillation mode is excited ($\beta_1 = 1$; $\beta_2 = 0$; $\beta_3 = 0$). For each subsystem (TAE or external load), the kinetic energy and potential energy change periodically with time: the increase of kinetic energy is accompanied with the decrease of potential energy. Since there is weak coupling between the two subsystems, small fluctuations are observed for \hat{E}_{TAE} and \hat{E}_L , however, their sum \hat{E}_T is invariant with time. In this condition, \hat{E}_L is much higher than \hat{E}_{TAE} which means that the external load has a much higher energy level. In Figure 15(b), at $K_M/K_b = 1$, both first and second oscillation modes are excited ($\beta_1 = 1$; $\beta_2 = 0.5$; $\beta_3 = 0$): quasi-periodicity occurs. The variations of $\hat{E}_{k,TAE}$, $\hat{E}_{p,TAE}$, $\hat{E}_{k,L}$ and $\hat{E}_{p,L}$ involve both first- and second-mode components, leading to irregular waveforms of \hat{E}_{TAE} and \hat{E}_L . In Figure 15(c), at $K_M/K_b = 4.5$, the first two oscillation modes are equally excited ($\beta_1 = 1$; $\beta_2 = 1$; $\beta_3 = 0$): beating oscillations happen. It is interesting to observe that, the beating effect also exists in the time histories of $\hat{E}_{k,TAE}$, $\hat{E}_{p,TAE}$, $\hat{E}_{k,L}$ and $\hat{E}_{p,L}$, resulting in periodic variations in \hat{E}_{TAE} and \hat{E}_L at a frequency of $f_2 - f_1$. In this case, the energy levels of TAE and external load are quite close. In Figure 15(d), at $K_M/K_b = 4.5$, all three oscillation modes are excited ($\beta_1 = 1$; $\beta_2 = 1$; $\beta_3 = 0.8$). Compared to Figure 15(c), the addition of quasi-periodicity makes the waveforms of \hat{E}_{TAE} and \hat{E}_L more complicated.

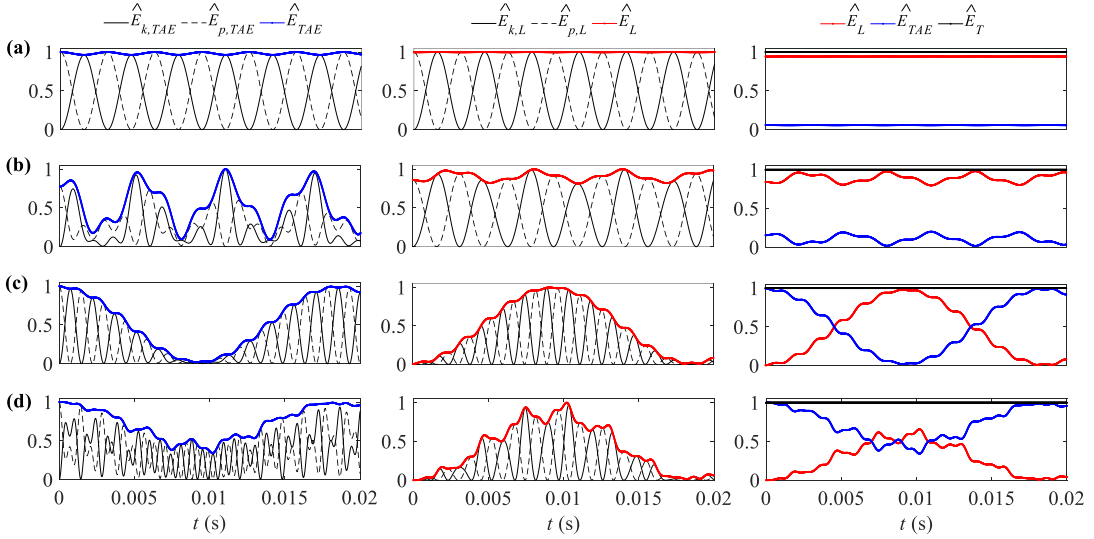


Figure 15. Energy transition at (a) $K_M/K_b = 1$, $\beta_1=1$; $\beta_2=0$; $\beta_3=0$. (b) $K_M/K_b = 1$, $\beta_1=1$; $\beta_2=0.5$; $\beta_3=0$. (c) $K_M/K_b = 4.5$, $\beta_1=1$; $\beta_2=1$; $\beta_3=0$. (d) $K_M/K_b = 4.5$, $\beta_1=1$; $\beta_2=1$; $\beta_3=0.8$.

The energy levels inside the TAE and external load at steady state can be quantified by the energy level ratio η_1 which is written as

$$\eta_1 = \bar{E}_L / \bar{E}_{TAE} \quad (24)$$

where \bar{E}_{TAE} and \bar{E}_L are time-averaged energy of the TAE and external load. Figure 16 illustrates the dependence of energy level ratio η_1 at single oscillation modes on the external load stiffness K_M . For example, the single first oscillation mode has $\beta_1 = 1; \beta_2 = 0; \beta_3 = 0$. Referring to Figure 4, we can find that, for each single oscillation mode, η_1 is large when the coupled frequency approximates f_M . If the coupled frequency approximates f_{TAE1} or f_{TAE2} , η_1 will decrease to very small values. Non-zero displacements at the right end are the major contributor for large values of η_1 . It can also be inferred from Figure 16 that, at a specified K_M , any mixture of oscillation modes (e.g., quasi-periodic oscillations) will have an overall value of η_1 between the maximum and minimum values of each single oscillation mode.

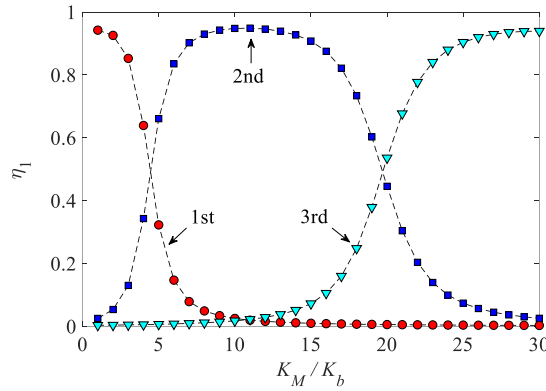


Figure 16. Effect of external load stiffness K_M on the energy level ratio η_1 at single oscillation modes.

6.2 Thermo-acoustic energy conversion

Apart from acousto-mechanical energy transition, the thermo-acoustic energy conversion between heat and acoustic energy inside the TAE is explored. The term “energy conversion” is adopted since heat and acoustic energy belong to different forms of energy.

In this work, we utilize the time-averaged acoustic power $W = \Re [p_i \tilde{U}_{1,i}]$ – to quantify thermo-acoustic coupling. The tilde “~” stands for complex conjugate. By using the network model, W along the TAE at each oscillation mode can be calculated. W at the fundamental mode has been investigated extensively in the literature (e.g., Figure (4) in Ref. [4]) and therefore not reproduced herein. Our calculations show that W at higher modes has similar shapes. Special attention is given to the acoustic power extraction ratio η_2 , which is defined as

$$\eta_2 = W(L) / \Delta W \quad (25)$$

where $W(L)$ represents acoustic power extraction by the external load and ΔW is acoustic power generation in the stack region. The larger η_2 is, the better energy conversion performance a thermoacoustic device has.

[Figure 17](#) illustrates the dependence of acoustic power extraction ratio η_2 at single oscillation modes on the external load stiffness K_M when r_h is fixed at 0.4 mm. The variation of η_2 at each single oscillation mode coincides with η_1 as K_M increases. Therefore, at a specified K_M , it is advantageous to excite the oscillation mode with large η_2 to achieve a large overall value.

[Figure 18](#) displays the dependence of $T_{h,\text{onset}}$ at single oscillation modes on K_M . Referring to [Figure 17](#), in the shaded region (I), initiation of the fundamental oscillation mode would lead to a large overall value of η_2 . In regions (II) and (III), to achieve large overall values, the second and third oscillation modes should be excited. However, $T_{h,\text{onset}}$ increases remarkably. This finding provides useful guidelines for the design and optimization of the external load, such as mechanical-to-electric transducer transducers. If the transducers are “noncompliant”, for example, $K_M/K_b > 30$, initiation of the oscillation mode with large η_2 seems impractical: $T_{h,\text{onset}}$ is too high. In most temperature ranges, only the fundamental mode is excited and the corresponding η_2 is very small (near zero) since the transducer is too “stiff” to move. This implies that most of the acoustic power produced is dissipated by the TAE itself. Therefore, it is beneficial to take advantage of region (I) by using “ultra-compliant” transducers. A recent study from Yu et al. [47] validates this idea by employing an ultra-compliant alternator for extracting the thermoacoustic power and achieved higher efficiencies.

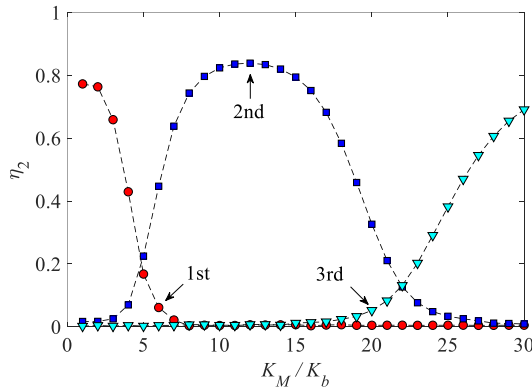


Figure 17. Effect of external load stiffness K_M on the acoustic power extraction ratio η_2 at single oscillation modes. r_h is fixed at 0.4 mm.

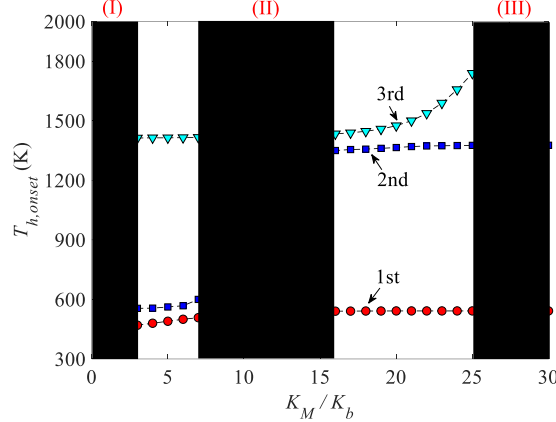


Figure 18. Effect of external load stiffness K_M on onset temperature $T_{h,\text{onset}}$ at single oscillation modes.
 r_h is fixed at 0.4 mm.

7. Conclusions

This paper endeavours to unveil the underlying mechanisms of various dynamic waveforms such as limit cycles, beating and quasi-periodicity, inside thermoacoustic devices. A lumped element model (LEM) is first established on a linear-type standing-wave thermoacoustic engine (TAE) integrated with an external load. The effect of acousto-mechanical coupling on the intrinsic oscillation modes is investigated. Then, a reduced-order network model is employed to study the effect of thermo-acoustic coupling on the stability of oscillation modes in the linear regime. Finally, the steady-state performance of the device is examined after inspecting the unsteady processes including linear decay/growth and nonlinear saturation.

From an acoustic/vibrational viewpoint, the acousto-mechanical coupling between the TAE and external load forms an eigenvalue problem, the solution of which determines the natural frequencies and mode shapes of the coupled system. From a thermodynamic/hydrodynamic viewpoint, the thermo-acoustic coupling between the temperature and acoustic fields in the stack region selects the linearly unstable oscillation mode(s). The linear mode selection decides whether the steady state is static or dynamic. Multiple oscillation modes can be damped/excited simultaneously in the linear decay/growth process. The nonlinear mode competition during the saturation process affects the dynamic steady-state responses as well.

Theoretical predictions show that when one single mode is excited, the steady-state waveforms are limit cycles. When two oscillation modes are initiated simultaneously, the steady-state waveforms could be either beating or quasi-periodic. The beating phenomenon arises when the natural frequency of the external load approximates the natural frequencies of the TAE. Otherwise, quasi-periodicity occurs. There could also exist situations where three oscillation modes are initiated simultaneously, resulting in more complex steady-state waveforms. Analyses on the steady-state energy transition and conversion

indicate that when the oscillation mode whose frequency approximates that of the external load is excited, the energy level ratio and acoustic power extraction ratio will have large values.

The LEM and network methodologies in this study provide useful tools for designing and optimising actual thermoacoustic generators, heat pumps and coolers, which normally consist of two or more subsystems and thus are acoustically complicated. They could also be used to study the active/passive control of thermoacoustic oscillations where a loudspeaker [48] or a stub [49] is often utilized to tune the acoustic fields inside the TAEs.

Acknowledgements

The authors want to acknowledge the Universitas 21 Doctoral Student Mobility Scholarship from the University of Auckland. The authors are also grateful for the financial support from China Scholarship Council (no. 201608630046). Fruitful discussions on the beating phenomena with Dr. Kai Wang at Imperial College London are highly appreciated.

Appendix A. Distributed parameter model

Consider an acoustic wave which is propagating in a lossless homogeneous medium. The acoustic pressure and velocity can be written as

$$\begin{cases} p_1 = A_1 e^{-jkx} + A_2 e^{jkx} \\ u_1 = \frac{1}{\rho_m a} (A_1 e^{-jkx} - A_2 e^{jkx}) \end{cases} \quad (\text{A1})$$

where $k = \omega/a$ denotes the wave number and a is the speed of sound. A_1 and A_2 are complex amplitudes of the right-running and left-running waves. Since there is a sudden change in cross-sectional area at the interfaces $x = x_l$ and $x = x_r$ where sound reflects and transmits, the acoustic resonator should be divided into three parts, as shown in Figure A1. The amplitudes of the right-running waves in parts A, B and C are p_{A1} , p_{B1} and p_{C1} , while the amplitudes of the left-running waves are p_{A2} , p_{B2} and p_{C2} .

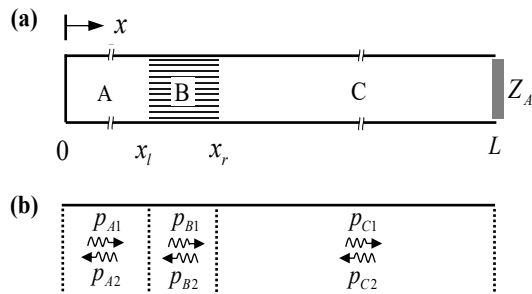


Figure A1. A distributed parameter model for validating the lumped element model.

At $x = 0$, the boundary condition is $u_1 = 0$. Thus,

$$p_{A1} = p_{A2} \quad (\text{A2})$$

At $x = x_l$, continuity of acoustic pressure and volume velocity gives

$$\begin{cases} p_{B1} = \frac{p_{A1}(e^{-j\kappa_l} + e^{j\kappa_l})S_1 + p_{A1}(e^{-j\kappa_l} - e^{j\kappa_l})S}{2e^{-j\kappa_l}S_1} \\ p_{B2} = \frac{p_{A1}(e^{-j\kappa_l} + e^{j\kappa_l})S_1 - p_{A1}(e^{-j\kappa_l} - e^{j\kappa_l})S}{2e^{j\kappa_l}S_1} \end{cases} \quad (\text{A3})$$

where S and S_1 are the cross-sectional areas in the parts A and B. Similarly, applying continuity of acoustic pressure and volume velocity at $x = x_r$, we have

$$\begin{cases} p_{C1} = \frac{(p_{B1}e^{-j\kappa_r} + p_{B2}e^{j\kappa_r})S + (p_{B1}e^{-j\kappa_r} - p_{B2}e^{j\kappa_r})S_1}{2e^{-j\kappa_r}S} \\ p_{C2} = \frac{(p_{B1}e^{-j\kappa_r} + p_{B2}e^{j\kappa_r})S - (p_{B1}e^{-j\kappa_r} - p_{B2}e^{j\kappa_r})S_1}{2e^{j\kappa_r}S} \end{cases} \quad (\text{A4})$$

Finally, at $x = L$, the equivalent acoustic impedance $Z_A = Z_L/S^2$ of the external load satisfies

$$Z_A = \frac{p_{C1}e^{-jkl} + p_{C2}e^{jkl}}{p_{C1}e^{-jkl} - p_{C2}e^{jkl}} \frac{\rho_m c}{S} \quad (\text{A5})$$

Solving this characteristic equation, we can obtain the natural frequencies of the coupled system. [Table A1](#) lists the natural frequencies calculated from both LEM and DPM methods at different values of external load stiffness. Good agreement is achieved between the results which verifies the LEM method used in this study.

Table A1. Comparison between the lumped element model and distributed parameter model on natural frequencies.

$K_M/K_b = 1$	$K_M/K_b = 4.5$	$K_M/K_b = 12$	$K_M/K_b = 20$	$K_M/K_b = 30$
LEM/DPM	LEM/DPM	LEM/DPM	LEM/DPM	LEM/DPM
f_1 (Hz)	159.3/160.1	309.8/311.1	332.2/335.1	333.4/336.3
f_2 (Hz)	340.3/342	363.7/362.6	549.8/546.5	681.9/678.1
f_3 (Hz)	708.3/709.1	708.8/705.9	711.4/707.6	736.3/730
				872.2/868.8

Appendix B. Thermodynamic/hydrodynamic analysis of thermoacoustic stack

Take an example of the onset temperature $T_{h,\text{onset}}$ of the first three oscillation modes versus r_h/δ_k at $K_M/K_b = 4.5$, as shown in [Figure B1](#). It shows that the optimal value of r_h/δ_k lies around 1.6. These results coincide with the conclusions drawn in a previous study [\[50\]](#).

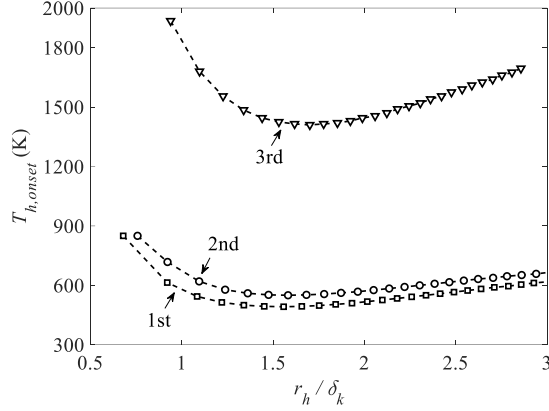


Figure B1. Dependence of onset temperature $T_{h,\text{onset}}$ on r_h/δ_k at $K_M/K_b = 4.5$.

To interpret the dependence of $T_{h,\text{onset}}$ on r_h/δ_k , the longitudinal time-averaged enthalpy flux h_x self-modulated in the vicinity of the plate surface is examined. According to the linear theory [1], h_x is the sum of time-averaged entropy flux and time-averaged work flux. It is expressed as

$$h_x = \rho_m c_p \Re[T_1 \tilde{t}_x] \quad (\text{A6})$$

where tilde “~” stands for the complex conjugate. The oscillating velocity u_1 and temperature T_1 are written as [1]

$$u_1 = -\frac{1}{j\omega\rho_m} (1-h_v) \frac{dp_1}{dx} \quad (\text{A7})$$

$$T_1 = \frac{1}{\rho_m c_p} (1-h_k) p_1 - \frac{1}{j\omega} \frac{dT_m}{dx} \frac{(1-h_k) - \sigma(1-h_v)}{(1-h_v)(1-\sigma)} u_1 \quad (\text{A8})$$

Subscripts “ m ” and “ 1 ” denote the mean and first-order expansion values of acoustic variables. $h_{v,k}$ are thermo-viscous functions of the parallel-plate thermoacoustic stack [43].

It is worth mentioning that actual value of h_x are affected by many factors such as mean temperature T_m , local temperature gradient dT_m/dx , thermophysical properties (μ, κ , etc.), and the acoustic field (p_1, u_1 , etc.). Because of this, the standing-wave assumption is adopted, i.e.

$$p_1 = A_1 \cos(kx); \quad u_1 = \frac{A_1}{j\rho_m a} \sin(kx)(1-h_v) \quad (\text{A9})$$

Moreover, normalized values of h_x are calculated. By doing these, the shape of \hat{h}_x is no longer sensitive to the factors mentioned above. As seen in Figure B2, \hat{h}_x peaks at $r_h/\delta_k \approx 1.6$ which matches with the optimal value predicted from the system-level network model. The close match qualitatively discloses the mechanism of optimal r_h/δ_k in thermoacoustic devices employing a parallel-plate thermoacoustic stack.

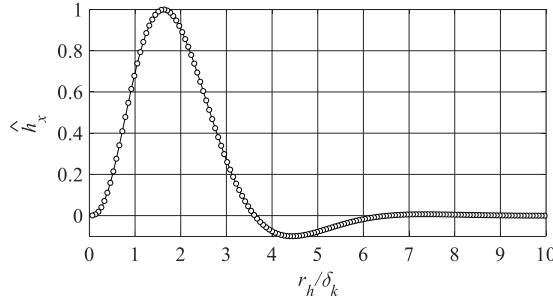


Figure B2. Dependence of dimensionless longitudinal time-averaged enthalpy flux $\langle \hat{h}_x \rangle_x$ on r_h/δ_k .

References

- [1] G.W. Swift, Thermoacoustics: A unifying perspective for some engines and refrigerators, Springer, 2017.
- [2] D. Zhao, Y. Chew, Energy harvesting from a convection-driven Rijke-Zhao thermoacoustic engine, Journal of Applied Physics, 112(11) (2012) 114507.
- [3] G. Chen, L. Tang, B.R. Mace, Modelling and analysis of a thermoacoustic-piezoelectric energy harvester, Applied Thermal Engineering, 150 (2019) 532-544.
- [4] G. Chen, L. Tang, Z. Yang, K. Tao, Z. Yu, An electret - based thermoacoustic - electrostatic power generator, International Journal of Energy Research, (2019).
- [5] H. Hao, C. Scalo, M. Sen, F. Semperlotti, Thermoacoustics of solids: A pathway to solid state engines and refrigerators, Journal of Applied Physics, 123(2) (2018) 024903.
- [6] H. Hao, C. Scalo, F. Semperlotti, Traveling and standing thermoacoustic waves in solid media, Journal of Sound and Vibration, 449 (2019) 30-42.
- [7] J.W.S.B. Rayleigh, The theory of sound, Macmillan, 1896.
- [8] N. Rott, Thermoacoustics, Advances in applied mechanics, 20 (1980) 135-175.
- [9] G. Swift, A. Migliori, J. Wheatley, Measurements with an optimized regenerator for a liquid - working - substance heat engine, Journal of applied physics, 54(12) (1983) 6834-6840.
- [10] J. Wheatley, T. Hofler, G. Swift, A. Migliori, Experiments with an intrinsically irreversible acoustic heat engine, Physical Review Letters, 50(7) (1983) 499.
- [11] P. Spoor, G. Swift, Thermoacoustic separation of a He-Ar mixture, Physical review letters, 85(8) (2000) 1646.

- [12] B. Ward, J. Clark, G. Swift, Design Environment for Low (amplitude Thermoacoustic Energy Conversion DeltaEC Version 6.3 b11 Users Guide, Los Alamos national laboratory, (2012).
- [13] G. Yu, E. Luo, W. Dai, J. Hu, Study of nonlinear processes of a large experimental thermoacoustic-Stirling heat engine by using computational fluid dynamics, *Journal of Applied Physics*, 102(7) (2007) 074901.
- [14] G. Chen, G. Krishan, Y. Yang, L. Tang, B. Mace, Numerical investigation of synthetic jets driven by thermoacoustic standing waves, *International Journal of Heat and Mass Transfer*, 146 (2020) 118859.
- [15] T. Biwa, Y. Tashiro, M. Ishigaki, Y. Ueda, T. Yazaki, Measurements of acoustic streaming in a looped-tube thermoacoustic engine with a jet pump, *Journal of applied physics*, 101(6) (2007) 064914.
- [16] P. Merkli, H. Thomann, Transition to turbulence in oscillating pipe flow, *Journal of Fluid Mechanics*, 68(3) (1975) 567-576.
- [17] T. Yazaki, A. Tominaga, Y. Narahara, Thermally driven acoustic oscillations: second-harmonic, *Physics Letters A*, 79(5-6) (1980) 407-409.
- [18] P. Gupta, G. Lodato, C. Scalo, Spectral energy cascade in thermoacoustic shock waves, *Journal of Fluid Mechanics*, 831 (2017) 358-393.
- [19] L. Qiu, D. Sun, Y. Tan, W. Yan, P. Chen, L. Zhao, G. Chen, Effect of pressure disturbance on onset processes in thermoacoustic engine, *Energy conversion and management*, 47(11) (2006) 1383-1390.
- [20] Y.-L. He, H.-B. Ke, F.-Q. Cui, W.-Q. Tao, Explanations on the onset and damping behaviors in a standing-wave thermoacoustic engine, *Applied Thermal Engineering*, 58(1) (2013) 298-304.
- [21] J. Tan, J. Wei, T. Jin, Onset and damping characteristics of a closed two-phase thermoacoustic engine, *Applied Thermal Engineering*, 160 (2019) 114086.
- [22] R. Delage, Y. Takayama, T. Biwa, On-off intermittency in coupled chaotic thermoacoustic oscillations, *Chaos: An Interdisciplinary Journal of Nonlinear Science*, 27(4) (2017) 043111.
- [23] Z. Yu, Q. Li, X. Chen, F. Guo, X. Xie, J. Wu, Investigation on the oscillation modes in a thermoacoustic Stirling prime mover: mode stability and mode transition, *Cryogenics*, 43(12) (2003) 687-691.
- [24] G. Penelet, T. Biwa, Synchronization of a thermoacoustic oscillator by an external sound source, *American Journal of Physics*, 81(4) (2013) 290-297.
- [25] T. Biwa, S. Tozuka, T. Yazaki, Amplitude death in coupled thermoacoustic oscillators, *Physical Review Applied*, 3(3) (2015) 034006.

- [26] H. Hyodo, T. Biwa, Phase-Locking and Suppression States Observed in Forced Synchronization of Thermoacoustic Oscillator, *Journal of the Physical Society of Japan*, 87(3) (2018) 034402.
- [27] G. Penelet, V. Gusev, P. Lotton, M. Bruneau, Experimental and theoretical study of processes leading to steady-state sound in annular thermoacoustic engines, *Physical Review E*, 72(1) (2005) 016625.
- [28] M. Guedra, G. Penelet, P. Lotton, Experimental and theoretical study of the dynamics of self-sustained oscillations in a standing wave thermoacoustic engine, *Journal of Applied Physics*, 115(2) (2014) 024504.
- [29] M. Chen, Y. Ju, Experimental study of quasi-periodic on-off phenomena in a small-scale traveling wave thermoacoustic heat engine, *Cryogenics*, 85 (2017) 23-29.
- [30] G. Penelet, E. Gaviot, V. Gusev, P. Lotton, M. Bruneau, Experimental investigation of transient nonlinear phenomena in an annular thermoacoustic prime-mover: observation of a double-threshold effect, *Cryogenics*, 42(9) (2002) 527-532.
- [31] Z. Yu, A.J. Jaworski, A.S. Abduljalil, Fishbone-like instability in a looped-tube thermoacoustic engine, *The Journal of the Acoustical Society of America*, 128(4) (2010) EL188-EL194.
- [32] T. Yazaki, S. Takashima, F. Mizutani, Complex quasiperiodic and chaotic states observed in thermally induced oscillations of gas columns, *Physical review letters*, 58(11) (1987) 1108.
- [33] T. Yazaki, Experimental observation of thermoacoustic turbulence and universal properties at the quasiperiodic transition to chaos, *Physical Review E*, 48(3) (1993) 1806.
- [34] T. Biwa, Y. Ueda, T. Yazaki, U. Mizutani, Thermodynamical mode selection rule observed in thermoacoustic oscillations, *EPL (Europhysics Letters)*, 60(3) (2002) 363.
- [35] A.A. Atchley, F.m. Kuo, Stability curves for a thermoacoustic prime mover, *The Journal of the Acoustical Society of America*, 95(3) (1994) 1401-1404.
- [36] V.R. Unni, Y.M. Prasaad, N. Ravi, S.M. Iqbal, B. Pesala, R. Sujith, Experimental investigation of bifurcations in a thermoacoustic engine, *International Journal of Spray and Combustion Dynamics*, 7(2) (2015) 113-129.
- [37] K. Wang, D. Sun, J. Zhang, N. Zhang, K. Luo, L. Qiu, Beating effect between a thermoacoustic source and its mechanical partner, *Journal of Applied Physics*, 118(24) (2015) 244907.
- [38] J. Olson, G. Swift, A loaded thermoacoustic engine, *The Journal of the Acoustical Society of America*, 98(5) (1995) 2690-2693.

- [39] D.-H. Li, Y.-Y. Chen, E.-C. Luo, Z.-H. Wu, Study of a liquid-piston traveling-wave thermoacoustic heat engine with different working gases, *Energy*, 74 (2014) 158-163.
- [40] M.A. Timmer, K. de Blok, T.H. van der Meer, Review on the conversion of thermoacoustic power into electricity, *The Journal of the Acoustical Society of America*, 143(2) (2018) 841-857.
- [41] G. Chen, L. Tang, B.R. Mace, Theoretical and experimental investigation of the dynamic behaviour of a standing-wave thermoacoustic engine with various boundary conditions, *International Journal of Heat and Mass Transfer*, 123 (2018) 367-381.
- [42] L. Fan, Z. Chen, J.-j. Zhu, J. Ding, J. Xia, S.-y. Zhang, H. Zhang, H. Ge, Nonlinear effects in a model of a thermoacoustic refrigerator driven by a loudspeaker, *Journal of Applied Physics*, 117(12) (2015) 124502.
- [43] W.P. Arnott, H.E. Bass, R. Raspet, General formulation of thermoacoustics for stacks having arbitrarily shaped pore cross sections, *The Journal of the Acoustical Society of America*, 90(6) (1991) 3228-3237.
- [44] K. Yang, J. Wang, D. Yurchenko, A double-beam piezo-magneto-elastic wind energy harvester for improving the galloping-based energy harvesting, *Applied Physics Letters*, 115(19) (2019) 193901.
- [45] W. Sutherland, LII. The viscosity of gases and molecular force, *The London, Edinburgh, and Dublin Philosophical Magazine and Journal of Science*, 36(223) (1893) 507-531.
- [46] T. Biwa, K. Sobata, S. Otake, T. Yazaki, Observation of thermoacoustic shock waves in a resonance tube, *The Journal of the Acoustical Society of America*, 136(3) (2014) 965-968.
- [47] Z. Yu, A.J. Jaworski, S. Backhaus, Travelling-wave thermoacoustic electricity generator using an ultra-compliant alternator for utilization of low-grade thermal energy, *Applied Energy*, 99 (2012) 135-145.
- [48] C. Olivier, G. Penelet, G. Poignand, P. Lotton, Active control of thermoacoustic amplification in a thermo-acousto-electric engine, *Journal of Applied Physics*, 115(17) (2014) 174905.
- [49] A. Kruse, T. Schmiel, M. Tajmar, Experimental validation of a looped-tube thermoacoustic engine with a stub for tuning acoustic conditions, *Energy Conversion and Management*, 177 (2018) 292-305.
- [50] Z. Yu, A. Jaworski, Optimization of thermoacoustic stacks for low onset temperature engines, *Proceedings of the Institution of Mechanical Engineers, Part A: Journal of Power and Energy*, 224(3) (2010) 329-337.